Axially Tailored Light Field by Means of a Dielectric Metalens

Xinhao Fan,[1] Peng Li,[1,*] Xuyue Guo,[1] Bingjie Li,[1] Yu Li,[1] Sheng Liu,[1] Yi Zhang,[2] and Jianlin Zhao[1,†]

[1] *MOE Key Laboratory of Material Physics and Chemistry under Extraordinary Conditions, and Shaanxi Key Laboratory of Optical Information Technology, School of Physical Science and Technology, Northwestern Polytechnical University, Xi'an 710072, China*

[2] *School of Chemical and Biomedical Engineering, Nanyang Technological University, 70 Nanyang Drive, Singapore, 637457, Singapore*

(Received 24 March 2020; revised 25 May 2020; accepted 10 July 2020; published 13 August 2020)

Metasurfaces that enable wave-front manipulation within the subwavelength range exhibit fascinating capabilities and application potentials in ultrathin functional devices. Therein, various metasurfaces to realize delicate transverse and even three-dimensional structured light fields have been proposed for applications such as holographic displays, imaging, optical manipulation, etc. However, a metasurface with the capability of tailoring the axial structure of a light field has not been reported so far. Here, we propose and experimentally demonstrate a dielectric metalens to tailor the axial intensity distribution of a light field, based on the independent control of amplitude and phase. The metalens is designed according to an optimized Fourier spectrum encoding method, which allows construction of an ultrasmall nondiffractive light field with any arbitrary preestablished axial structure. This axial modulation scenario enriches the three-dimensional wave-front modulation functionality of the metasurface, and can be implemented for other waves beyond optics, from acoustic and elastic waves to matter waves.

DOI: 10.1103/PhysRevApplied.14.024035

I. INTRODUCTION

Metasurfaces are artificially ultrathin materials formed by two-dimensional arrays of subwavelength structures, which can modify the amplitude, phase, and polarization distribution of electromagnetic waves on a subwavelength scale [1]. Therefore, in recent years, they have been extensively studied to develop miscellaneous devices, such as lenses [2], wave plates [3], holograms [4], polarization detectors [5], multiplexers [6], and so on [7]. The valid response of metasurfaces has been expanded from the microwave to the visible spectrum [8]. According to the actuating medium, metasurfaces can be classified into two categories, metallic and dielectric [9,10]. The former category has prominent capabilities at microwave and THz frequencies [11–13], as well as a nonlinear effect [14–16]. The latter category, which consists of materials with high refractive indices, currently attracts considerable interest, and has been widely designed into various transmission-type devices, because of the advantages of low loss, magnetic response, and managed dispersion at optical frequencies [17–27]. Most impressively, achromatic metalenses with high numerical aperture (NA) and efficiency have been developed in depth for near-infrared and visible frequencies [28–30]. However, the highly efficient transmission brings about another issue, that is, how to modulate the amplitude parameter. To address this problem, dielectric metasurfaces commonly encode the amplitude information of wave front into their phase functions, using phase-only computer-generated holograms [31–33]. Unfortunately, the accompanying background noise is another issue.

Recently, some transmission-type metal metasurfaces consisting of split rings and multilayer meta-atoms [34,35] and dielectric metasurfaces with distinctive geometric elements have been demonstrated with the capability of independent control of amplitude and phase [36,37]. The full control of complex amplitude of a light field creates significant improvements in holographic display, flexible manipulation of diffraction, and so on. It is noteworthy that, although various metasurfaces for modulating the transverse and three-dimensional (3D) distribution of the light field have been successfully proposed, a metasurface aiming to tailor the axial structure of a light field has not been reported so far.

Here, we propose a single-layer dielectric metalens for axially tailoring a light field. The metalens is designed according to an optimized Fourier spectrum encoding method. It consists of an array of rectangular nanopillars

*pengli@nwpu.edu.cn
†jlzhao@nwpu.edu.cn

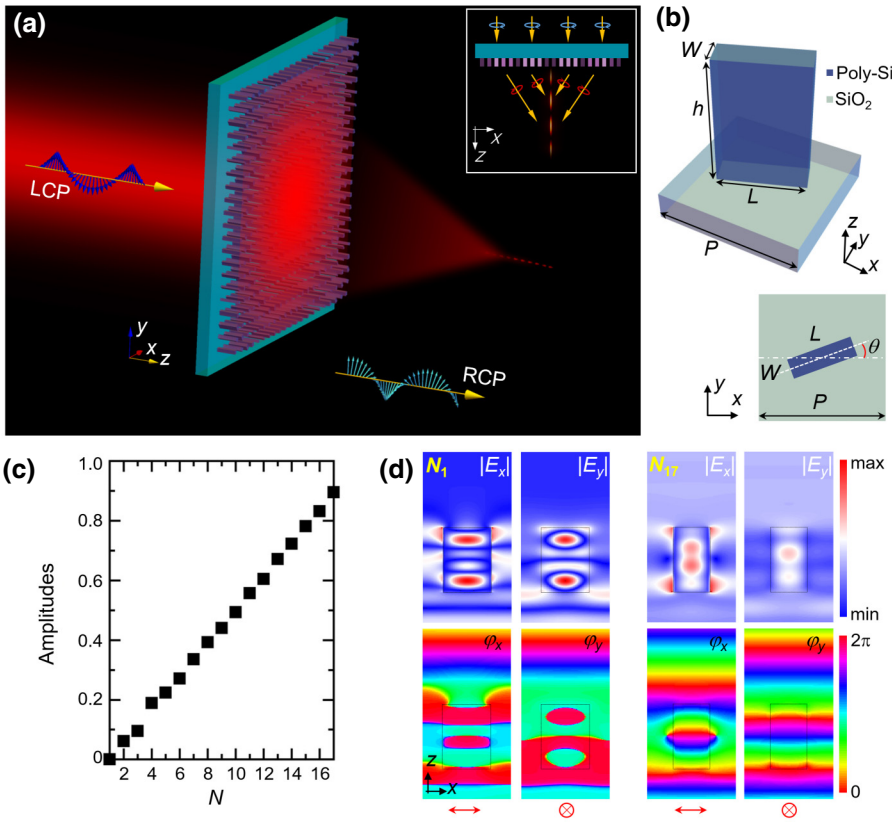

FIG. 1. Design of dielectric metalens with independent control of amplitude and phase. (a) Schematic of axial tailoring of light field via a single-layer dielectric metalens. Inset: sketch of the illumination details. For the normal incidence of a circularly polarized beam, the metalens transforms it into an oppositely polarized beam with radially varying transmission amplitude (denoted by rectangles with different brightness) and phase, then generates an axially tailored field. (b) Top: meta-atom of poly-Si nanopillar deposited on SiO_2 substrate with geometric parameters of L (length), W (width), h (height), and P (period). Bottom: top view of the meta-atom. θ is the rotation angle of the rectangular nanopillar relative to the reference coordinate system. (c) Transmission amplitudes of 17 selected geometries. (d) Normalized electric fields and phase distributions when x- and y-polarized light beams illuminate the 1st (N_1) and 17th (N_{17}) geometries. The red arrows and crosses depict the polarization orientations of incident light beams.

with various geometric parameters and rotation angles, which allow the complete and independent control of amplitude and phase. As shown in Fig. 1(a), for an incident circularly polarized light field, the metalens transforms it into an oppositely polarized field with radially variant transmission amplitude and phase, which focuses into an ultrasmall nondiffractive light field with preestablished intensity profile along the propagating direction, namely performing the axial tailoring of the light field. To validate our proposed approach, we successfully fabricate two metalenses and observe the construction of nondiffractive fields with uniform and oscillating profiles.

II. METALENS DESIGN

A. Independent control of amplitude and phase

To realize the independent control of amplitude and phase, we start by analyzing the response of a dielectric metasurface that consists of subwavelength meta-atoms with the simplest geometry, that is, a rotated rectangular nanopillar, as reported in Ref. [37]. As shown in Fig. 1(b), the meta-atom is a rotated rectangular nanopillar with high refractive index deposited on a transparent substrate, whose period and geometric parameters are denoted by P and h (height), L (length), W (width), and θ (rotation angle), respectively. The high-index nanopillar can be considered as a truncated waveguide, which has corresponding effective refractive indices for two orthogonal linearly polarized components. Hence, this rotated rectangular nanopillar performs wave-front modulation as a birefringent element. Suppose that the transmission amplitude and phase delay are denoted as T_0 and δ, respectively. Thus the Jones matrix of such an element can be expressed as

$$\mathbf{J} = T_0 e^{i\varphi_0} R(-\theta) \begin{bmatrix} e^{i\delta/2} & 0 \\ 0 & e^{-i\delta/2} \end{bmatrix} R(\theta), \qquad (1)$$

where $R(\cdot)$ is the rotation matrix and $\varphi_0 = (\varphi_e + \varphi_o)/2$ denotes the propagation phase depending on the accumulated phases of two linearly polarized components (φ_e and φ_o correspond to the extraordinary and ordinary components, respectively). As a result, for the incidence of a circularly polarized beam, whose polarization is described as $[1\ i]^{\mathrm{T}}$, the output field can be expressed as

$$\mathbf{E} = \frac{T_0 e^{i\varphi_0}}{\sqrt{2}} \cos\frac{\delta}{2} \begin{bmatrix} 1 \\ i \end{bmatrix} + i \frac{T_0 e^{i\varphi_0}}{\sqrt{2}} \sin\frac{\delta}{2} e^{i2\theta} \begin{bmatrix} 1 \\ -i \end{bmatrix}. \qquad (2)$$

Equation (2) clearly shows that the output field contains two components with orthogonally circular polarizations. The first component has the same polarization as the incident beam; in other words, it is the directly transmitted component, whose amplitude is strongly dependent on $\cos(\delta/2)$. And yet the second component has an opposite circular polarization, whose complex amplitude can be

expressed as $T_0 \sin(\delta/2)\exp[i(\varphi_0+2\theta)]$. According to this, a dielectric metasurface consisting of similar geometric elements has been proposed recently to realize the independent control of amplitude and phase, whose elements have constant T_0 and φ_0 but varying δ and θ [37]. That is, the second output component has modulated amplitude and phase depending on δ and θ, respectively. Nevertheless, once the desired amplitude is not equal to 1, i.e., $\sin(\delta/2)\neq 1$, according to Eq. (2), then $\cos(\delta/2)\neq 0$. This means that this metasurface has a significant directly transmitted component. Therefore, a circular polarization filter is required in front of the observer [37].

Here, eliminating the coaxially transmitted component, namely the first term on the right-hand side of Eq. (2), is the precondition for realizing axial modulation. According to Eq. (2), we find that, when $\delta=\pm\pi$, the element acts as a half-wave plate, i.e., $\cos(\delta/2)=0$ and $\sin(\delta/2)=\pm 1$, by which the incident beam can be totally transformed into the opposite polarization in theory, that is, the directly transmitted component is eliminated. Therefore, the transmission complex amplitude can be expressed as $T_0\exp[i(\varphi_0+2\theta)]$. Obviously, the amplitude of the output field is only dependent on the transmission efficiency of the element, which is determined by the geometric size. The phase function is related to the combination of propagation and geometric phases, i.e., φ_0 and 2θ. To break this correlation, we here introduce an indirect parameter, which is defined as $\theta'=\theta-\varphi_0/2$. Consequently, in practice, we eliminate the propagation phase by adding an opposite rotation angle of $\varphi_0/2$ on θ. Therefore, the output light field has independently modulated amplitude and phase, which are tunable by steering the geometric parameters and rotation angle of the meta-atom, respectively.

According to this principle, we choose polycrystalline silicon (poly-Si) and SiO_2 as high-refractive-index material and substrate, then scan the length and width of the nanopillar to pick out 17 geometries, for which the phase delay is near to π as much as possible (see Fig. S1 and Sec. 1 of the Supplemental Material [38]). The corresponding transmission amplitudes are shown in Fig. 1(c). It can be seen from this diagram that these selected geometries present a good linear relationship. As an example, Fig. 1(d) displays the amplitude and phase distribution of normalized electric fields in the x-z plane, when x- and y-polarized light beams illuminate the 1st (N_1) and 17th (N_{17}) selected geometries, respectively. The rotation angles of the two geometries are both $\theta=0$. The black dashed rectangles depict the interfaces of nanopillars. These results are numerically calculated by using finite-difference time-domain (Lumerical software) simulation. The incident wavelength is 670 nm and the thicknesses of the poly-Si and substrate are 570 nm and 500 μm, respectively. The geometric sizes of N_1 are found to be $L=W=220$ nm. As shown, for this geometry, the destructive interference of forward scattered fields induces near-zero transmission amplitude [39], i.e., $E_0\approx 0$. While

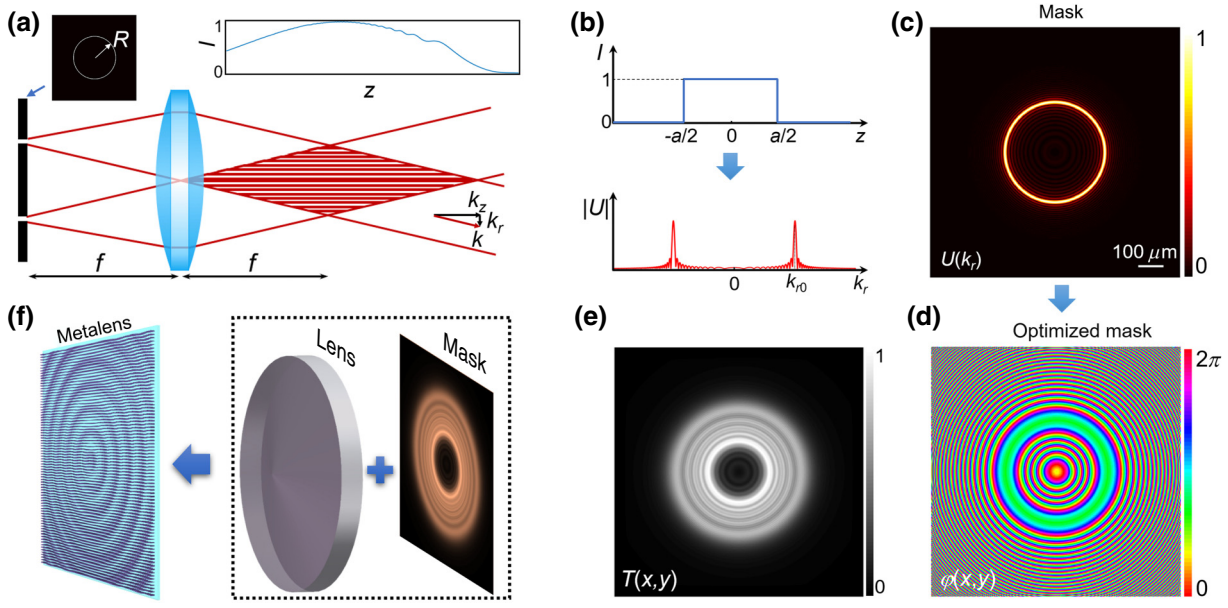

FIG. 2. Assembling a dielectric metalens for axially tailoring a light field. (a) Schematic of generating Bessel beam based on Durnin ring. Inset: Durnin ring mask with a sharp transparent ring and the corresponding normalized intensity profile on the z axis. (b) Preestablished intensity profile $I(r=0,z)$ (top) on the axis and amplitude distribution of the corresponding spatial spectrum $U(k_r)$ (bottom). (c) Transmission distribution of the Fourier spectrum mask. The mask sizes are 1.08×1.08 mm^2. (d) Phase and (e) amplitude distribution of the optimized mask calculated from the spatial spectrum, according to Eq. (5). (f) Assembly diagram of metalens from the Fourier transform lens and optimized mask.

for the N_{17} geometry, whose geometric sizes are found to be $L = 166$ nm and $W = 112$ nm, the transmission amplitudes of the two components are obviously enhanced. These results exhibit the tunability of transmission amplitude by changing the nanopillar geometry.

B. Axial tailoring theory

We employ the spatial spectrum optimization method of Durnin ring to implement the axial modulation [40, 41]. The operation principle is schematically shown in Fig. 2(a). For this method, a Durnin ring mask with a sharp transparent ring, whose radius is R, is placed at the front focal plane of a Fourier lens, so the incident light beam passing through this mask generates a quasi-Bessel beam in the space near the back focal plane of the lens, with a Gaussian-like intensity profile on the z axis, as shown in the inset of Fig. 2(a). The Durnin ring and the Bessel beam have a relationship of $R/f = \sqrt{k^2 - k_z^2}/k_z$, where f denotes the focal length of the lens and k_z is the propagation constant of the Bessel beam. This corresponding relationship has been introduced into dielectric gradient metalenses to design axicons with high efficiencies [42–44], which can only generate ultrasmall Bessel beams with axial profiles similar to that of the inset in Fig. 2(a).

In cylindrical coordinates, a light field with arbitrary axial intensity function $[I(z) = |E(z)|^2]$ can be decomposed into orthogonal Bessel spectra with different propagation constants k_z as [40]

$$E(r = 0, z) = \int_0^k U\left(\sqrt{k^2 - k_z^2}, z\right) \exp(ik_z z) k_z dk_z, \quad (3)$$

where $E(r = 0,z)$ denotes the preestablished axial amplitude function, $U(\cdot)$ corresponds to the coefficient of the Bessel spectrum, and $k = 2\pi/\lambda$ is the wave number. According to the inverse Fourier transform of Eq. (3), the spatial spectrum thus can be expressed as

$$U\left(\sqrt{k^2 - k_z^2}, z = 0\right) = \frac{1}{2\pi k_z} \mathcal{F}^{-1}\{E(z) \exp(ik_{z0} z)\}, \quad (4)$$

where $\mathcal{F}^{-1}\{\cdot\}$ denotes the inverse Fourier transform function and k_{z0} is the propagation constant corresponding to the main spatial spectrum. Considering the Fourier transform relationship between the Bessel and delta functions, the complex coefficient in Eq. (4) actually represents the complex amplitude at the Fourier spectrum plane, which replaces the sharp transparent ring. Figure 2(b) illustrates the Fourier spectrum optimization principle of an axial rectangle function, i.e., $E(r = 0, z) = \mathrm{rect}(z/a)$, with a denoting the width of the rectangle function. The lower diagram in Fig. 2(b) depicts the radial amplitude distribution of the optimized spatial spectrum. Figure 2(c) displays the transmission distribution of the corresponding mask.

To design a compact metalens integrated with Fourier transform functionality, the transmission function at the front focal plane, that is, the complex amplitude function expressed in Eq. (4), is replaced by a transfer function that contains the propagation process from the front focal plane to the surface of the lens, which can be described as the Fresnel diffraction of the light field in Eq. (4) as

$$U(x, y) = T(x, y) e^{i\varphi(x,y)} \propto \mathcal{F}\left\{\frac{1}{2\pi k_z} \mathcal{F}^{-1}\{E(z) \exp(ik_{z0} z)\} \exp\left(ik \frac{x_0^2 + y_0^2}{2f}\right)\right\}. \quad (5)$$

Figures 2(d) and 2(e) display the phase and amplitude distribution of the optimized complex transmission, i.e., $U(x,y)$, which is calculated from Fig. 2(c) according to Eq. (5). The assembly of the metasurface is schematically shown in Fig. 2(f) (see Sec. 2 of the Supplemental Material [38]).

III. EXPERIMENTAL RESULTS AND DISCUSSION

Figures 3(a) and 3(b) display scanning electric microscopy (SEM) images of the metalens fabricated according to the theory discussed above. As shown in Fig. 3(b), nanopillars present radially variant geometries and rotation angles with a period of 450 nm, indicating the radial variation of transmission. The pixel sizes of the metasurface are 2400 × 2400.

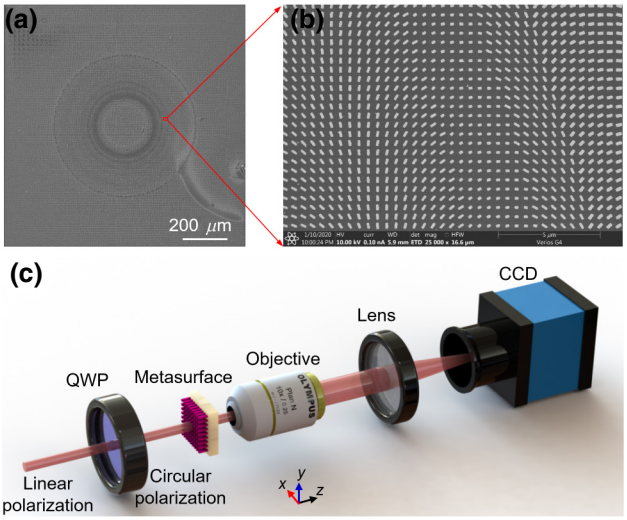

FIG. 3. (a) SEM image of the metalens and (b) its locally enlarged image. This metalens is fabricated for generating a nondiffractive light field with rectangular intensity profile along the z axis. (c) Experimental setup. QWP: quarter-wave plate. The microscopic measurement system consisting of objective and tube lenses and CMOS camera is placed on a linear translation stage that moves along the z direction.

This single-layer dielectric metalens is fabricated based on the processes of deposition, patterning, liftoff, and etching. At first, a 570-nm-thick poly-Si film is deposited on a 500-μm-thick SiO_2 substrate by inductively coupled plasma enhanced chemical vapor deposition, and then a 100-nm-thick hydrogen silsesquioxane electron beam spin-on resist (HSQ, XR-1541) is spin-coated onto the poly-Si film and baked on a hot plate at 100 °C for 2 min. Next, the desired structures are imprinted by using standard electron beam lithography (Nanobeam Limited, NB5) and subsequently developed in NMD-3 solution (concentration of 2.38%) for 2 min. Finally, the desired structures are transferred from the resist to the poly-Si film by using inductively coupled plasma etching (Oxford Instruments, Oxford Plasma Pro 100 Cobra300).

Figure 3(c) shows the experimental setup. A linearly polarized beam from a diode-pumped solid-state laser with a wavelength of 670 nm is normally incident onto the metalens, after passing through a quarter-wave plate. The desired light fields with longitudinally tailored intensity and ultrasmall transverse scale are generated after the metasurface. We use a microscopic measurement system consisting of a 10× objective lens (NA = 0.25), tube lens (f = 20 cm), and CMOS camera with a resolution of 2048 × 2048 and pixel size of 5.5 × 5.5 μm^2 (acA2040, Basler) to characterize such special fields. The microscopic measurement system is fixed on a linear translation stage to implement the z-scanned measurement and to map the 3D intensity distributions. In experiments, we set the back surface of the metasurface as the $z = 0$ plane.

We first assess the axial tailoring capability by observing the reconstructed light field from the metalens shown in Fig. 3(a), which is designed and fabricated by using parameters f = 3 mm, a = 2 mm, and R_0 = 200 μm. The numerically reconstructed intensity distribution in the y-z plane and the on-axis intensity profile are shown in Figs. 4(a) and 4(b), respectively. These intensity distributions are normalized. As shown, this metalens supports the construction of a nondiffractive light field, which presents a rectangular intensity profile with slight disturbance in the range from $z = 2$ to 4 mm. The disturbance is induced by the deficiency of high-order spatial spectrum, because the aperture of the metalens limits the Bessel components with large transverse wave vector.

Figure 4(c) displays the experimentally measured 3D intensity distribution in a longitudinal range from $z = 1.6$ to 4.2 mm, which is mapped from the scanned data with an interval of 10 μm. Considering the rotational symmetry of the reconstructed light field, we set the $x = 0$ plane as a front surface to intuitively present the intensity distribution near the z axis. Figure 4(d) shows the measured on-axis intensity distribution. Figure 4(e) displays the transverse normalized intensity distributions at four planes corresponding to the red points shown in Fig. 4(d). Consistent with the theoretical prediction, this experimentally

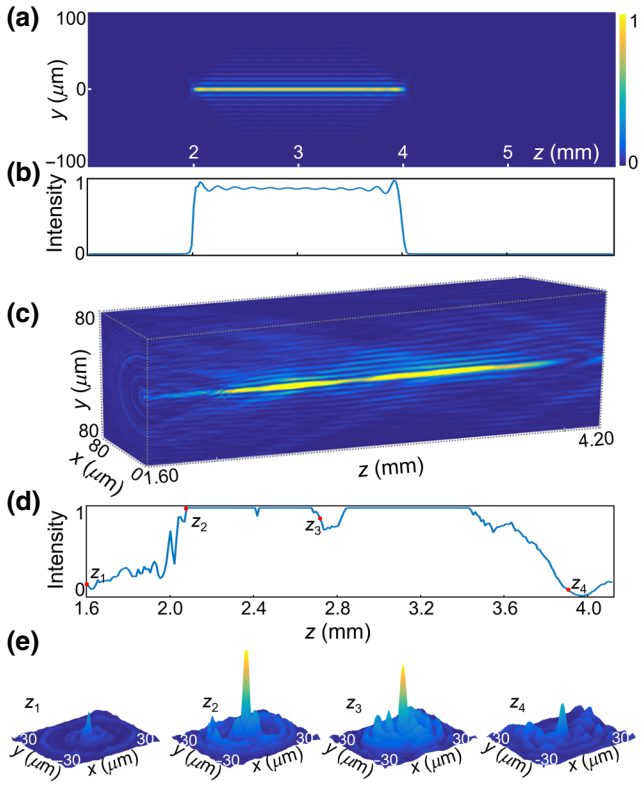

FIG. 4. Normalized intensity distributions of a rectangle-profiled light field. (a) Numerically reconstructed light field in the y-z plane. (b) Calculated on-axis intensity distribution. (c) Measured 3D intensity distribution in a longitudinal interval of 2.6 mm. (d) Measured on-axis intensity distribution. Red points: z_1 = 1.6 mm, z_2 = 2.1 mm, z_3 = 2.7 mm, and z_4 = 3.9 mm. (e) Measured intensity distributions at the planes of z_1, z_2, z_3, and z_4.

constructed light field retains its transverse width (half-width of the main lobe is about 4 μm) in a longitudinal interval of about 2 mm, namely showing a quasi-zeroth-order nondiffractive light field in such a distance. Moreover, in contrast to the slowly varying intensity profile shown in the inset of Fig. 2(a), Fig. 4(d) clearly shows a steep rising edge and a relatively slow descending edge near the $z = 2$ and 4 mm planes, respectively, indicating the successful generation of an axially tailored light field from the metalens. Note that the intensity patterns in Fig. 4(e) clearly show that, besides the zeroth-ordered main lobe, these high-ordered lobes follow the preestablished variation along the z direction likewise. This means that the generated light beam has a nondiffractive property, which is of great significance for optical processing [45].

To validate the flexibility and universality of this axial tailoring concept, we design other structured light fields. Figure 5(a) shows the spatial spectrum of a light field with axially oscillating intensity on the z axis, i.e., $E(z) = \cos(2\pi bz)$, with b denoting the oscillating period.

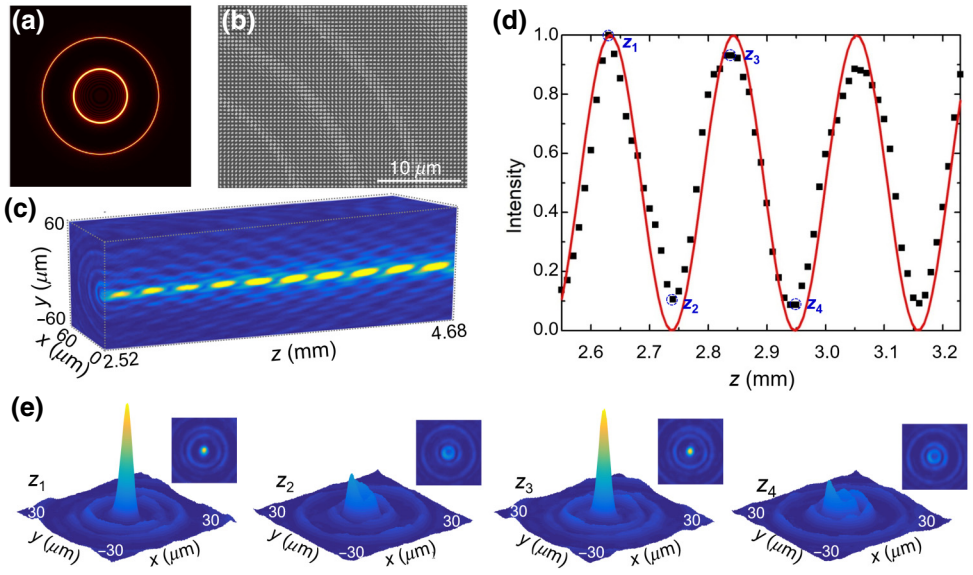

FIG. 5. Measurement of oscillating field constructed from metalens. (a) Transmission distribution of the mask corresponding to a cosinusoidal profile. (b) Local SEM image of the metalens. (c) Measured 3D intensity distribution in a longitudinal interval from $z = 2.52$ to 4.68 mm. (d) Measured on-axis intensity and the corresponding fitted curve. (e) Transverse intensity distributions at four planes corresponding to the points shown in (d). Insets: top-view intensity patterns. These intensity distributions are normalized.

According to the assembly method, we design and fabricate a metalens, a SEM image of which is shown in Fig. 5(b). Figure 5(c) displays the experimentally measured intensity distribution in a longitudinal range from $z = 2.52$ to 4.68 mm. Intuitively, the on-axis intensity presents an oscillating profile. Figure 5(d) shows the measured intensity distribution on the axis, where the black squares and red curve represent the measured results and the fit to the data, respectively. The experimental results are in good agreement with the theory, presenting a cosinusoidal curve with a period of about 210 μm. Figure 5(e) displays the intensity distributions in a square region near the axis at four transverse planes, whose longitudinal positions are denoted by the dashed circles on the cosinusoidal curve shown in Fig. 5(d), corresponding to these four adjacent peak and valley points. Different from the results shown in Fig. 4(e), this beam periodically varies its transverse pattern with the oscillation of on-axis intensity, presenting a "light cage" structure in 3D space, which has been reported as having application potential in particle trap and manipulation [46], as well as imaging [47,48]. The longitudinal period is discussed in Sec. 3 of the Supplemental Material [38].

Besides the compactness, another advantage provided by the full control of complex amplitude is the transmission efficiency. Compared with the Fourier spectrum mask shown in Fig. 2(c), which is commonly used in traditional optical devices such as spatial light modulator because of the single response of amplitude and phase [40,41], the optimized mask can significantly enlarge the transmitted area of the mask. Consequently, the generation efficiency is enhanced from 3.8% to about 19.8%. These efficiencies are estimated by integrating the transmittances. It is noteworthy that, in the experiment, the size of the Durnin ring is adjustable to match the focus and the preestablished axial structure, so that the transmitted area can be as large as possible, resulting in the improvement of the generation efficiency. Whereas, the efficiency is strongly dependent on the preestablished profile, e.g., the efficiency of the oscillating field is about 6.3%. Actually, the cosine profile can be decomposed as the coherent superposition of two Bessel beams with different transverse wave vectors. Consequently, the spectrum mask consists of just two rings, as shown in Fig. 5(a). On the other hand, for a light field with a complex axial profile, more spectrum rings can enhance the efficiency.

In addition, both the transverse and longitudinal structures of these proposed light fields can be further reduced, by combining our method with a high-NA metalens, to create structured light fields with subwavelength geometries [49], and even superoscillating fields [50], providing fruitful opportunities for applications in optical processing, imaging, particle manipulation, and so on. Use of such an axially oscillating field is a pioneering approach for constructing tightly focusing fields with longitudinally oscillating polarization [51]. Furthermore, this kind of axial modulation scenario based on metasurfaces can be implemented in other waves beyond optics, from acoustic waves [52] to matter waves [53].

IV. CONCLUSION

In conclusion, we propose a single-layer dielectric metalens with independent control of amplitude and phase to achieve the axial tailoring of a light field. Based on the full control of complex amplitude of the light field, we design and fabricate metalenses according to an optimized Fourier spectrum encoding method, which enable the construction of nondiffractive fields with any arbitrary preestablished

axial intensity profiles. As demonstration, ultrasmall nondiffractive light fields with axially uniform and oscillating intensities are experimentally generated. This ultraflat and ultrasmall metalens enriches the 3D modulation of light fields at ultrasmall scale, and could be further investigated in relation to other waves.

ACKNOWLEDGMENTS

This work is supported by National Natural Science Foundation of China (NSFC) (11634010, 91850118, 11774289, 61675168), National Key Research and Development Program of China (2017YFA0303800), Fundamental Research Funds for the Central Universities (3102018zy036, 3102019JC008), and Seed Foundation of Innovation and Creation for Graduate Students in Northwestern Polytechnical University, China (ZZ2019220). We thank the Analytical and Testing Center of Northwestern Polytechnical University.

[1] H. T. Chen, A. J. Taylor, and N. Yu, A review of metasurfaces: Physics and applications, Rep. Prog. Phys. **79**, 076401 (2016).

[2] M. Khorasaninejad and F. Capasso, Metalenses: Versatile multifunctional photonic components, Science **358**, eaam8100 (2017).

[3] N. Yu, F. Aieta, P. Genevet, M. A. Kats, Z. Gaburro, F. Capasso, and A. Broadband, Background-Free quarter-wave plate based on plasmonic metasurfaces, Nano Lett. **12**, 6328 (2012).

[4] D. Wen, F. Yue, G. Li, G. Zheng, K. Chan, S. Chen, M. Chen, K. F. Li, P. W. H. Wong, K. W. Cheah, E. Yue Bun Pun, S. Zhang, and X. Chen, Helicity multiplexed broadband metasurface holograms, Nat. Commun. **6**, 8241 (2015).

[5] N. A. Rubin, G. D'Aversa, P. Chevalier, Z. Shi, W. T. Chen, and F. Capasso, Matrix Fourier optics enables a compact full-stokes polarization camera, Science **365**, eaax1839 (2019).

[6] S. Chen, W. Liu, Z. Li, H. Cheng, and J. Tian, Metasurface-Empowered optical multiplexing and multifunction, Adv. Mater. **32**, 1805912 (2020).

[7] J. Sung, G. Y. Lee, and B. Lee, Progresses in the practical metasurface for holography and lens, Nanophotonics **8**, 1701 (2019).

[8] S. Sun, Q. He, J. Hao, S. Xiao, and L. Zhou, Electromagnetic metasurfaces: Physics and applications, Adv. Opt. Photonics **11**, 380 (2019).

[9] N. Meinzer, W. L. Barnes, and I. R. Hooper, Plasmonic meta-atoms and metasurfaces, Nat. Photonics **8**, 889 (2014).

[10] M. Choudhury Sajid, D. Wang, K. Chaudhuri, C. DeVault, V. Kildishev Alexander, A. Boltasseva, and M. Shalaev Vladimir, Material platforms for optical metasurfaces, Nanophotonics **7**, 959 (2018).

[11] Q. Wang, X. Zhang, E. Plum, Q. Xu, M. Wei, Y. Xu, H. Zhang, Y. Liao, J. Gu, J. Han, and W. Zhang, Polarization and frequency multiplexed terahertz meta-holography, Adv. Opt. Mater. **5**, 1700277 (2017).

[12] K. Chaudhuri, A. Shaltout, D. Shah, U. Guler, A. Dutta, V. M. Shalaev, and A. Boltasseva, Photonic spin hall effect in robust phase gradient metasurfaces utilizing transition metal nitrides, ACS Photonics **6**, 99 (2019).

[13] X. Fu, F. Yang, C. Liu, X. Wu, and T. J. Cui, Terahertz beam steering technologies: From phased arrays to field-programmable metasurfaces, Adv. Opt. Mater. **8**, 1900628 (2019).

[14] G. Li, S. Zhang, and T. Zentgraf, Nonlinear photonic metasurfaces, Nat. Rev. Mater. **2**, 17010 (2017).

[15] S. Chen, G. Li, W. Cheah Kok, T. Zentgraf, and S. Zhang, Controlling the phase of optical nonlinearity with plasmonic metasurfaces, Nanophotonics **7**, 1013 (2018).

[16] W. Y. Tsai, T. L. Chung, H. H. Hsiao, J. W. Chen, R. J. Lin, P. C. Wu, G. Sun, C. M. Wang, H. Misawa, and D. P. Tsai, Second harmonic light manipulation with vertical split ring resonators, Adv. Mater. **31**, 1806479 (2019).

[17] S. Jahani and Z. Jacob, All-dielectric metamaterials, Nat. Nanotechnol. **11**, 23 (2016).

[18] S. M. Kamali, E. Arbabi, A. Arbabi, and A. Faraon, A review of dielectric optical metasurfaces for wavefront control, Nanophotonics **7**, 1041 (2018).

[19] M. I. Shalaev, J. Sun, A. Tsukernik, A. Pandey, K. Nikolskiy, and N. M. Litchinitser, High-Efficiency All-dielectric metasurfaces for ultracompact beam manipulation in transmission mode, Nano Lett. **15**, 6261 (2015).

[20] M. A. Ansari, I. Kim, D. Lee, M. H. Waseem, M. Zubair, N. Mahmood, T. Badloe, S. Yerci, T. Tauqeer, M. Q. Mehmood, and J. Rho, A spin-encoded All-dielectric metahologram for visible light, Laser Photonics Rev. **13**, 1900065 (2019).

[21] W. T. Chen, A. Y. Zhu, J. Sisler, Z. Bharwani, and F. Capasso, A broadband achromatic polarization-insensitive metalens consisting of anisotropic nanostructures, Nat. Commun. **10**, 355 (2019).

[22] A. Arbabi, Y. Horie, A. J. Ball, M. Bagheri, and A. Faraon, Subwavelength-thick lenses with high numerical apertures and large efficiency based on high-contrast transmitarrays, Nat. Commun. **6**, 7069 (2015).

[23] L. Jin, Z. Dong, S. Mei, Y. F. Yu, Z. Wei, Z. Pan, S. D. Rezaei, X. Li, A. I. Kuznetsov, Y. S. Kivshar, J. K. W. Yang, and C. W. Qiu, Noninterleaved metasurface for (26-1) spin- and wavelength-encoded holograms, Nano Lett. **18**, 8016 (2018).

[24] I. Kim, G. Yoon, J. Jang, P. Genevet, K. T. Nam, and J. Rho, Outfitting next generation displays with optical metasurfaces, ACS Photonics **5**, 3876 (2018).

[25] G. Y. Lee, J. Y. Hong, S. Hwang, S. Moon, H. Kang, S. Jeon, H. Kim, J.-H. Jeong, and B. Lee, Metasurface eyepiece for augmented reality, Nat. Commun. **9**, 4562 (2018).

[26] R. Zhao, B. Sain, Q. Wei, C. Tang, X. Li, T. Weiss, L. Huang, Y. Wang, and T. Zentgraf, Multichannel vectorial holographic display and encryption, Light Sci. Appl. **7**, 95 (2018).

[27] H. Ren, G. Briere, X. Fang, P. Ni, R. Sawant, S. Héron, S. Chenot, S. Vézian, B. Damilano, V. Brändli, S. A. Maier, and P. Genevet, Metasurface orbital angular momentum holography, Nat. Commun. **10**, 2986 (2019).

[28] S. Wang, P. C. Wu, V. C. Su, Y. C. Lai, C. Hung Chu, J. W. Chen, S. H. Lu, J. Chen, B. Xu, C. H. Kuan, T. Li, S. Zhu, and D. P. Tsai, Broadband achromatic optical metasurface devices, Nat. Commun. **8**, 187 (2017).

[29] E. Arbabi, A. Arbabi, S. M. Kamali, Y. Horie, and A. Faraon, Controlling the sign of chromatic dispersion in diffractive optics with dielectric metasurfaces, Optica **4**, 625 (2017).

[30] G. H. Yuan, E. T. F. Rogers, and N. I. Zheludev, Achromatic super-oscillatory lenses with sub-wavelength focusing, Light Sci. Appl. **6**, e17036 (2017).

[31] Z.-L. Deng and G. Li, Metasurface optical holography, Mater. Today Phys. **3**, 16 (2017).

[32] D. Wen, F. Yue, W. Liu, S. Chen, and X. Chen, Geometric metasurfaces for ultrathin optical devices, Adv. Opt. Mater. **6**, 1800348 (2018).

[33] X. Guo, P. Li, J. Zhong, S. Liu, B. Wei, W. Zhu, S. Qi, H. Cheng, and J. Zhao, Tying polarization-switchable optical vortex knots and links via holographic All-dielectric metasurfaces, Laser Photonics Rev. **14**, 1900366 (2020).

[34] J. Ding, S. An, B. Zheng, and H. Zhang, Multiwavelength metasurfaces based on single-layer dual-wavelength meta-atoms: Toward complete phase and amplitude modulations at Two wavelengths, Adv. Opt. Mater. **5**, 1700079 (2017).

[35] H. X. Xu, G. Hu, L. Han, M. Jiang, Y. Huang, Y. Li, X. Yang, X. Ling, L. Chen, J. Zhao, and C. W. Qiu, Chirality-Assisted high-efficiency metasurfaces with independent control of phase, amplitude, and polarization, Adv. Opt. Mater. **7**, 1801479 (2019).

[36] G. Y. Lee, G. Yoon, S. Y. Lee, H. Yun, J. Cho, K. Lee, H. Kim, J. Rho, and B. Lee, Complete amplitude and phase control of light using broadband holographic metasurfaces, Nanoscale **10**, 4237 (2018).

[37] A. C. Overvig, S. Shrestha, S. C. Malek, M. Lu, A. Stein, C. Zheng, and N. Yu, Dielectric metasurfaces for complete and independent control of the optical amplitude and phase, Light Sci. Appl. **8**, 92 (2019).

[38] See Supplemental Materical at http://link.aps.org/supplemental/10.1103/PhysRevApplied.14.024035 for geometry selection of nanopillars, design of metalens, and longitudinal period of tailored field.

[39] D. Sikdar, W. Cheng, and M. Premaratne, Optically resonant magneto-electric cubic nanoantennas for ultra-directional light scattering, J. Appl. Phys. **117**, 083101 (2015).

[40] P. Li, Y. Zhang, S. Liu, L. Han, H. Cheng, F. Yu, and J. Zhao, Quasi-Bessel beams with longitudinally varying polarization state generated by employing spectrum engineering, Opt. Lett. **41**, 4811 (2016).

[41] T. Čižmár and K. Dholakia, Tunable bessel light modes: Engineering the axial propagation, Opt. Express **17**, 15558 (2009).

[42] D. Lin, P. Fan, E. Hasman, and M. L. Brongersma, Dielectric gradient metasurface optical elements, Science **345**, 298 (2014).

[43] W. T. Chen, M. Khorasaninejad, A. Y. Zhu, J. Oh, R. C. Devlin, A. Zaidi, and F. Capasso, Generation of wavelength-independent subwavelength bessel beams using metasurfaces, Light Sci. Appl. **6**, e16259 (2017).

[44] Z. Ma, S. M. Hanham, P. Albella, B. Ng, H. T. Lu, Y. Gong, S. A. Maier, and M. Hong, Terahertz All-dielectric magnetic mirror metasurfaces, ACS Photonics **3**, 1010 (2016).

[45] M. Duocastella and C. B. Arnold, Bessel and annular beams for materials processing, Laser Photonics Rev. **6**, 607 (2012).

[46] M. Mazilu, D. J. Stevenson, F. Gunn-Moore, and K. Dholakia, Light beats the spread: "non-diffracting" beams, Laser Photonics Rev. **4**, 529 (2010).

[47] G. Antonacci, G. D. Domenico, S. Silvestri, E. DelRe, and G. Ruocco, Diffraction-free light droplets for axially-resolved volume imaging, Sci. Rep. **7**, 17 (2017).

[48] L. Gao, L. Shao, B. C. Chen, and E. Betzig, 3D live fluorescence imaging of cellular dynamics using bessel beam plane illumination microscopy, Nat. Protocols **9**, 1083 (2014).

[49] H. Hu, Q. Gan, and Q. Zhan, Generation of a Nondiffracting Superchiral Optical Needle for Circular Dichroism Imaging of Sparse Subdiffraction Objects, Phys. Rev. Lett. **122**, 223901 (2019).

[50] G. Yuan, K. S. Rogers, E. T. F. Rogers, and N. I. Zheludev, Far-Field Superoscillatory Metamaterial Superlens, Phys. Rev. Appl. **11**, 064016 (2019).

[51] P. Li, X. Fan, D. Wu, S. Liu, Y. Li, and J. Zhao, Self-accelerated optical activity in free space induced by gouy phase, Photon. Res. **8**, 475 (2020).

[52] B. Assouar, B. Liang, Y. Wu, Y. Li, J. C. Cheng, and Y. Jing, Acoustic metasurfaces, Nat. Rev. Mater. **3**, 460 (2018).

[53] Y. Yang, G. Thirunavukkarasu, M. Babiker, and J. Yuan, Orbital-Angular-Momentum Mode Selection by Rotationally Symmetric Superposition of Chiral States with Application to Electron Vortex Beams, Phys. Rev. Lett. **119**, 094802 (2019).